RSC Advances

ROYAL SOCIETY OF CHEMISTRY

PAPER

View Article Online
View Journal | View Issue

Cite this: *RSC Adv.*, 2024, **14**, 9791

Controllable fabrication of CoNi bimetallic alloy for high-performance electromagnetic wave absorption†

Hai Xie,[abc] Jinmei Li,[ac] Rui Yang,[ac] Juan Yang,[d] Tingmei Wang*[abc] and Qihua Wang *[abc]

With the coming era of artificial intelligence (AI) dominated by high-tech electronics, developing high-performance microwave absorption materials (MAMs) is imperative to solve the problem of increasing electromagnetic inference and pollution. Herein, a metal–organic framework (MOF)-derived CoNi bimetallic alloy (CoNi/C) with an irregular rod-like structure is prepared by a thermal reduction method. Introducing the CoNi alloy facilitates the balance between conduction loss and polarization loss and forms good impedance matching, leading to excellent microwave absorption performance. Interestingly, the optimization of absorption performance can be further achieved by controllably modulating the molar ratio of Co and Ni (Co^{2+}/Ni^{2+}). As expected, the obtained CoNi/C delivers excellent microwave absorption performance with a minimum reflection loss (RL_{min}) of −50.80 dB at 10.40 GHz and an effective absorption bandwidth (EAB) of 3.28 GHz (8.91–12.19 GHz) with a filler loading of 50 wt% at 2.0 mm. In addition, the CoNi/C can reach a maximum EAB of 4.77 GHz (12.99–17.76 GHz) at a low thickness of 1.5 mm, spanning nearly the entire Ku band. The $CoNi_3$/C also exhibits an impressive RL_{min} of −44.84 dB at 3.28 GHz in the S band. This work offers a novel strategy to modulate the magnetic/electric properties of MOF-derived MAMs.

Received 27th December 2023
Accepted 14th March 2024

DOI: 10.1039/d3ra08896k

rsc.li/rsc-advances

1. Introduction

The considerable electromagnetic inference and pollution generated by the widespread application of electromagnetic radiation have negatively affected electronic devices, information security, living environments, and human health.[1–5] Currently, the development of suitable microwave absorption materials (MAMs) that can interact with electromagnetic waves and convert microwave energy into thermal energy is a promising approach to mitigate electromagnetic radiation.[6–8] Excellent MAMs should have the advantages of "reducing weight, small coating thickness, broadening absorption, and strong reflection loss".[3,9–11] Despite the satisfactory microwave absorption performance of traditional MAMs, they have limited attenuation capacity, low dielectric loss capability, and poor impedance matching due to single polarization, making it difficult for them to reach the requirements.[9,12,13] Therefore, it is of great significance to develop excellent MAMs.

In recent years, alloys have been widely studied as important MAMs because of their favorable magnetic properties, good thermal and electrical conductivity, and high strength.[14] Among the various alloys, the CoNi alloy has drawn considerable attention for its low cost, excellent magnetic loss properties, and desirable microwave absorption characteristics.[15–17] However, the CoNi alloy has a high density and therefore cannot fulfill the needs of lightweight systems.[15,17] In addition, as many papers reported, the CoNi alloys mostly suffer from mismatching electromagnetic parameters, resulting in poor electromagnetic wave absorption performance.[15,18,19] It is highly desirable to explore a suitable precursor for the construction of CoNi alloys.

Metal–organic frameworks (MOFs) have been considered ideal candidates for the preparation of MAMs due to their tunable chemical composition and structure, hierarchical pore structure, good electromagnetic coordination and attenuation, and easy locking of dielectric/magnetic combinations.[9,20–22] Currently, MOF-derived MAMs (carbon/metal oxide hybrids, carbon/metal hybrids, *etc.*) have made great progress in electromagnetic wave absorption with their excellent impedance matching and microwave loss characteristics.[23,24] Therefore,

[a]*Key Laboratory of Science and Technology on Wear and Protection of Materials, Lanzhou Institute of Chemical Physics, Chinese Academy of Sciences, Lanzhou, 730000, China. E-mail: wangqh@licp.cas.cn; tmwang@licp.cas.cn*

[b]*Center of Materials Science and Optoelectronics Engineering, University of Chinese Academy of Sciences, Beijing, 100049, China*

[c]*State Key Laboratory of Solid Lubrication, Lanzhou Institute of Chemical Physics, Chinese Academy of Sciences, Lanzhou, 730000, China*

[d]*Laboratory of Clean Energy Chemistry and Materials, State Key Laboratory of Solid Lubrication, Lanzhou Institute of Chemical Physics, Chinese Academy of Sciences, Lanzhou, 730000, China*

† Electronic supplementary information (ESI) available. See DOI: https://doi.org/10.1039/d3ra08896k

developing high-performance CoNi alloys derived from MOFs is a viable strategy, but remains a great challenge.

Herein, we report the fabrication of a CoNi alloy anchored on carbon nanorods (CoNi/C) as an efficient MAM. By adjusting the molar ratio of Co and Ni (Co^{2+}/Ni^{2+}), the components and electromagnetic wave absorption performance of the CoNi alloy can be effectively controlled. Additionally, benefiting from the configuration of the CoNi alloy and strong interfacial interactions between CoNi and carbon nanorod, the as-prepared CoNi/C with a 50 wt% paraffin loading possesses exhibits a minimum reflection loss (RL_{min}) of −50.80 dB at a thickness of 2.0 mm. The $CoNi_3$/C also delivers an impressive RL_{min} of −44.84 dB at 3.28 GHz in the S band. Meanwhile, the effective absorption bandwidth (EAB) of CoNi/C reaches a maximum of 4.77 GHz at a low thickness of 1.5 mm, covering nearly the whole Ku band frequency. The combination of the electrical loss of carbon and the magnetic loss of the NiCo alloy can optimize impedance matching of CoNi/C, effectively widening the absorbing band of the composite. This work opens up a promising strategy for the synthesis of MOF-derived alloy/carbon composites with high-performance.

2. Experimental

2.1 Synthesis of CoNi-MOF precursors

The CoNi-MOF precursors were synthesized by a facile one-pot method. Briefly, 0.02 mol $Co(NO_3)_2 \cdot 6H_2O$ and 0.02 mol $Ni(NO_3)_2 \cdot 6H_2O$ were dissolved in 240 mL ethyl alcohol by ultrasonic treating. Then 2.00 mmol terephthalic acid (PTA) was added under stirring. Subsequently, the above mixed solution was kept stirring in an oil bath at 80 °C for 120 min. After cooling, the solvent was evaporated by rotary evaporation. Finally, the resulting CoNi-MOF was dried at 60 °C for 12 h.

For comparison, CoNi-MOF-1 and CoNi-MOF-2 were synthesized when the molar ratios of Co^{2+} and Ni^{2+} were modulated to 3 : 1 and 1 : 3, respectively, under the same preparation conditions.

2.2 Synthesis of CoNi/C composites

In a typical synthesis, the resulting CoNi-MOF, CoNi-MOF-1, and CoNi-MOF-2 were placed in a quartz boat and annealed under an atmosphere of 10% H_2–90% Ar at 600 °C for 4 h with a heating rate of 2 °C min^{-1} to obtain CoNi/C, Co_3Ni/C, and $CoNi_3$/C, respectively.

For comparison, CoNi/C-500 and CoNi/C-700 were prepared by pyrolysis in a 10% H_2–90% Ar atmosphere at 500 and 700 °C for 4 h, respectively, with a heating rate of 2 °C min^{-1}.

2.3 Characterization

The morphologies of samples were characterized by scanning electron microcopy (SEM, JSM-6700) and high-resolution transmission electron microscopy (TEM, JEM-3010). The crystal structure, pore structure, and chemical state of samples were analyzed using X-ray diffractometer (XRD, Shimadzu XRD-7000), Brunauer–Emmett–Teller (BET, Quantachrome Autosorb-iQ), and X-ray photoelectron spectroscopy (XPS, JPS-9010 MC), respectively.

2.4 Microwave absorption and electromagnetic parameters measurement

To investigate the electromagnetic wave absorption performance, the mixture of sample and paraffin (50 wt% mass loading) was pressed into testing ring with an inner diameter of 3 mm and an outer diameter of 7 mm. Additionally, CoNi/C-40 and CoNi/C-60 were prepared by uniformly mixing CoNi/C in the paraffin with filler loading of 40 wt% and 60 wt%, respectively. The electromagnetic parameters of samples could be detected by a PNA-L Vector Network Analyzer (Keysight, N5232B) over the range of 2–18 GHz. The RL value of samples was calculated by the transmission line theory:[25–27]

$$Z_{in} = Z_0\sqrt{\frac{\mu_r}{\varepsilon_r}}\tanh\left[j\left(\frac{2\pi fd}{c}\right)\sqrt{\varepsilon_r\mu_r}\right] \quad (1)$$

$$RL(dB) = 20\log\left|\frac{Z_{in}-Z_0}{Z_{in}+Z_0}\right| \quad (2)$$

where Z_{in} is the input impedance of the absorber, μ_r and ε_r are the complex permeability and permittivity, respectively. Z_0 is impedance of free space, d is the absorber's thickness, c and f represent the light velocity in the free space and the frequency of microwave, respectively.

3. Results and discussion

3.1 Material synthesis and structural characterizations

The detailed synthesis procedure of the CoNi/C composites is illustrated in Fig. 1. First, Co^{2+} and Ni^{2+} could coordinate with PTA and obtain CoNi-MOF precursors. In a pyrolysis process with an atmosphere of H_2–Ar (10% H_2), CoNi-MOF precursors could be transformed into CoNi alloys with an irregular rod-like structure.

As shown in Fig. 2a and b, SEM image reveals that the CoNi/C consists of many irregular nanorods. It can be seen that Co_3Ni/C and $CoNi_3$/C exhibit a rod-like structure similar to that of CoNi/C (Fig. S1†). TEM image (Fig. 2c) also shows the same morphology. As depicted in Fig. 2d, the microstructure of CoNi/C is further investigated by the high-resolution TEM (HRTEM). The inverse fast Fourier transform (IFFT) pattern (the inset in Fig. 2d) and the line profiles (Fig. 2e) display a lattice fringe spacing of 0.207 nm, which corresponds to the (111) plane of $Co_{0.5}Ni_{0.5}$ (PDF#04-004-8490). In addition, the selected area electron diffraction (SAED) pattern of CoNi/C shows bright diffraction spots aligned in a line (Fig. 2f), indicating the single crystalline structure of CoNi/C. The diffraction spots are indexed to (200), (220), and (020) planes of CoNi alloy, which is in accordance with the XRD results. As shown in Fig. 2g–k, the elemental mapping images of CoNi/C indicate that the elements of C, O, Co, and Ni are homogeneously distributed on the CoNi/C surface.

Furthermore, XRD spectra were conducted to determine the lattice structures of CoNi-MOF, Co_3Ni/C, CoNi/C, and $CoNi_3$/C

Fig. 1 Schematic illustration of the synthesis process of CoNi/C composites.

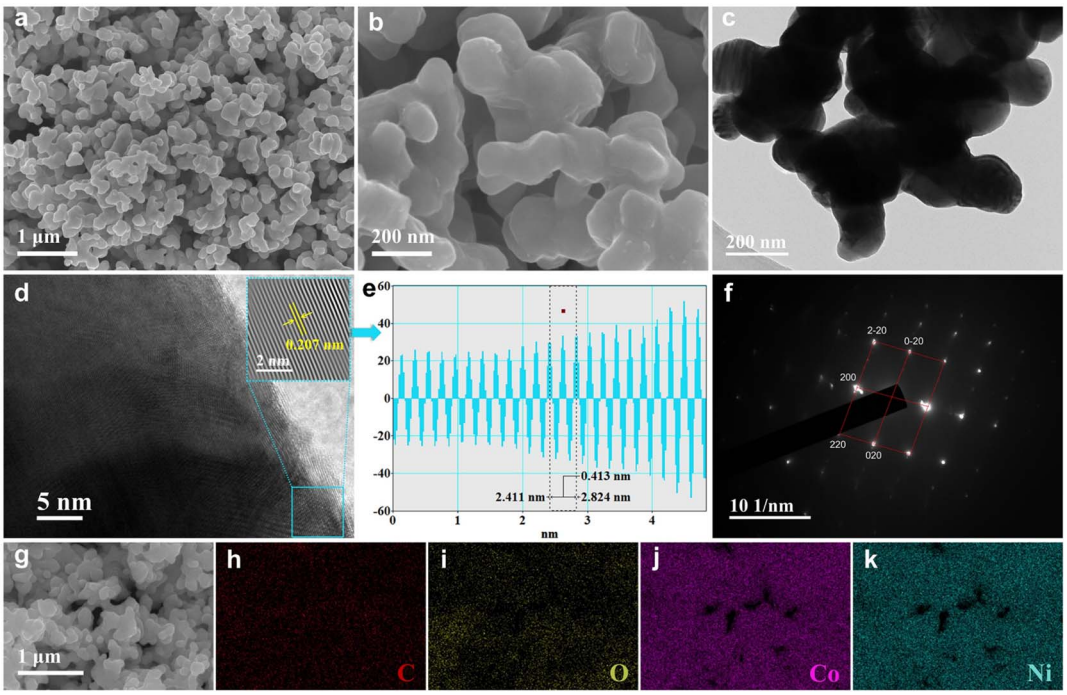

Fig. 2 Structural analyses of CoNi/C. (a and b) SEM images. (c) TEM image. (d) HRTEM image. Inset of (d) is the FFT pattern. (e) The line profiles in panel (d). (f) SAED pattern. (g) Elemental mapping distributions for C (h), O (i), Co (j), and Ni (k) of CoNi/C.

composites. XRD pattern displays the characteristic diffraction peaks of CoNi-MOF (Fig. S2†). As depicted in Fig. 3, the diffraction peaks located at 44.4°, 51.7°, and 76.1° are corresponding to the (111), (200), and (220) planes of $Co_{0.5}Ni_{0.5}$ (PDF#04-004-8490), confirming the formation of CoNi alloy. This result is consistent with the TEM results, further demonstrating that constructing CoNi alloys *via* CoNi-MOF precursors is an effective strategy. In addition, CoNi/C-500 and CoNi/C-700 exhibit a crystal structure similar to that of CoNi/C (Fig. S3†).

To reveal the elemental compositions and chemical state of CoNi/C, the XPS is performed. As depicted in Fig. 4a, XPS survey spectrum of CoNi/C detects obvious signals of C 1s, O 1s, Co 2p, and Ni 2p, which is coincident with the results of elemental mapping analysis. In addition, the atomic contents of Co and Ni elements can be found to be 10.93 at% and 11.15 at%, respectively, which are close to the initial feed ratios. The C and O elements possess high atomic contents of 44.69% and 33.23% in the CoNi/C, respectively. The XPS analysis results further indicate a slight reduction in the atomic content of Co and Ni as the pyrolysis temperature increases (Fig. S4 and Table S1†). As shown in Fig. 4b, the high-resolution C 1s spectrum shows the two peaks at 284.6 and 285.7 eV, ascribing to the C–C and C–O bonds, respectively.[2,16,28] The high-resolution Co 2p spectrum in Fig. 4c shows two pairs of doublet peaks located at 775–790 eV and 792–805 eV, which can be attributed to Co $2p_{3/2}$ and Co $2p_{1/2}$, respectively.[29] For the Co $2p_{3/2}$ spin–orbit, three main peaks located at 779.2, 781.2, and 786.3 eV can be assigned to the Co^0, Co^{2+}, and satellite signal peaks, respectively.[30] Likewise, Ni $2p_{3/2}$

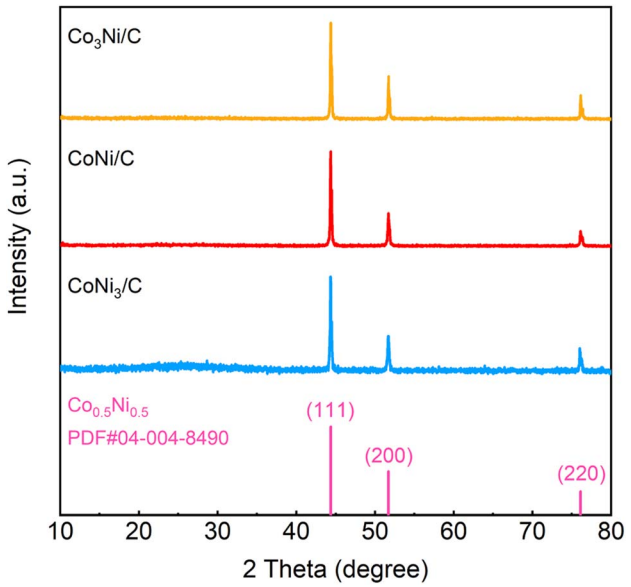

Fig. 3 XRD patterns of Co_3Ni/C, CoNi/C, and $CoNi_3/C$.

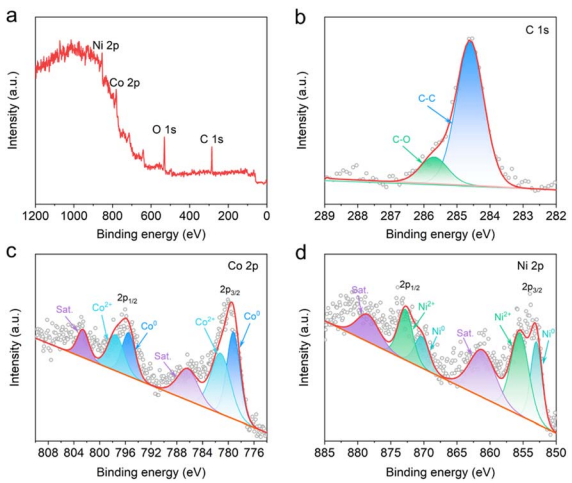

Fig. 4 XPS spectra of CoNi/C. (a) Survey spectrum. High-resolution (b) C 1s, (c) Co 2p, and (d) Ni 2p spectra.

XPS spectrum of CoNi/C (Fig. 4d) displays three peaks located at 853.0, 855.5, and 861.2 eV, corresponding to the Ni^0, Ni^{2+}, and satellite signal peaks, respectively.[29,31] The existence of metallic Co^0 and Ni^0 proves the formation of CoNi bimetallic alloy.[32] Besides, the peaks of Co^{2+} and Ni^{2+} are also defected, demonstrating the presence of metal oxidation states. This result is attributed to the formation of a high valence oxide passivation layer due to the unavoidable oxidation on the surface of nanoalloys.[28,33,34] The pore structure of CoNi/C was measured by BET analysis. The CoNi/C shows type-IV isotherms with a type H3 hysteresis loop, implying the presence of mesoporous (Fig. S5†). The BET surface area of CoNi/C is 52.3 $m^2\ g^{-1}$ with a main pore size of approximately 4.3 nm.

3.2 Electromagnetic wave absorption performance

The RL and EAB values are important parameters for evaluating the electromagnetic wave absorption performance of nanomaterials.[10] The calculated RL values of Co_3Ni/C, CoNi/C, and $CoNi_3/C$ are shown in Fig. 5a–i. Co_3Ni/C, with a low thickness of 1.5 mm, exhibits a strong RL_{min} of −40.08 dB at 14.98 GHz and a maximum EAB of 4.40 GHz (13.20–17.60 GHz) with a filler loading of 50 wt% (Fig. 5a). Under the same filler mass, the CoNi/C demonstrates an optimal RL_{min} of −50.80 dB at 10.40 GHz with a low thickness of 2.0 mm and a maximum EAB of 4.77 GHz (12.99–17.76 GHz) at 1.5 mm (Fig. 5b). As depicted in Fig. 5c, the RL_{min} of $CoNi_3/C$ reaches −44.84 dB at 3.28 GHz in the S band and the maximum EAB is 3.48 GHz (10.65–14.13 GHz). The corresponding three-dimensional (3D) and contour RL representations of Co_3Ni/C, CoNi/C, and $CoNi_3/C$ are shown in Fig. 5d–i. In addition, CoNi/C-500, CoNi/C-700, CoNi/C-40, and CoNi/C-60 exhibit the RL_{min} values of −13.66 dB at 17.12 GHz (thickness of 1.5 mm), −22.02 dB at 14.04 GHz (thickness of 2.0 mm), −20.34 dB at 5.92 GHz (thickness of 5.0 mm), and −35.35 dB at 16.52 GHz (thickness of 2.0 mm), respectively (Fig. S6 and S7†). The corresponding EAB values of CoNi/C-500, CoNi/C-700, CoNi/C-40, and CoNi/C-60 are measured to be 2.88, 3.48, 5.82, and 5.96 GHz, respectively. The results indicate that the CoNi/C exhibits excellent electromagnetic wave absorption performance and broad EAB, surpassing most advanced MOF-based absorbers reported in the literature (Table S2†).

To investigate the mechanism of electromagnetic wave absorption, the real parts (ε' and μ'), imaginary parts (ε'' and μ''), dielectric loss tangent ($\tan\delta_\varepsilon$), and magnetic loss tangent ($\tan\delta_\mu$) are displayed in Fig. 6. Generally, the real parts represent the storage ability of the electric and magnetic energy and imaginary parts denote the loss capability, such as energy dissipation, dielectric and magnetic loss.[2,35,36] Fig. 6a and b show the complex dielectric constants of Co_3Ni/C, CoNi/C, and $CoNi_3/C$. In the frequency range of 2.0–18.0 GHz, the ε' values of Co_3Ni/C, CoNi/C, and $CoNi_3/C$ decrease from 14.8 to 10.8, 12.8 to 10.4 and 19.0 to 15.3, respectively, illustrating a decreasing trend with increasing frequency. This result is related to the frequency dispersion behavior.[37] It is worth noting that the Co_3Ni/C, CoNi/C, and $CoNi_3/C$ display obvious relaxation peaks at ~11.6, 13.9, and 7.9 GHz, respectively, which can be attributed to the polarization behaviors at CoNi alloy/C heterogeneous interface.[37,38] In addition, it is found that the $\tan\delta_\varepsilon$ value of CoNi/C is higher than that of $CoNi_3/C$ in the frequency range between 12.0 and 16.0 GHz (Fig. 6c), indicating a higher polarization loss capability.[37] As shown in Fig. 6d–f, it can be seen that the CoNi/C has the high μ and μ'' values in the frequency range below 7.8 GHz, demonstrating its good impedance matching.[39] Meanwhile, the $\tan\delta_\mu$ values of the Co_3Ni/C, CoNi/C, and $CoNi_3/C$ display a similar trend with the μ'' values. Compared with the $\tan\delta_\varepsilon$ values of CoNi/C, it can be concluded that the loss of CoNi/C are mainly from magnetic loss in the frequency range of 2.0–11.9 GHz, while in 12.0–18.0 GHz mainly comes from dielectric loss. Similarly, it can be observed that the $\tan\delta_\mu$ values of Co_3Ni/C and $CoNi_3/C$ are higher than the $\tan\delta_\varepsilon$ values

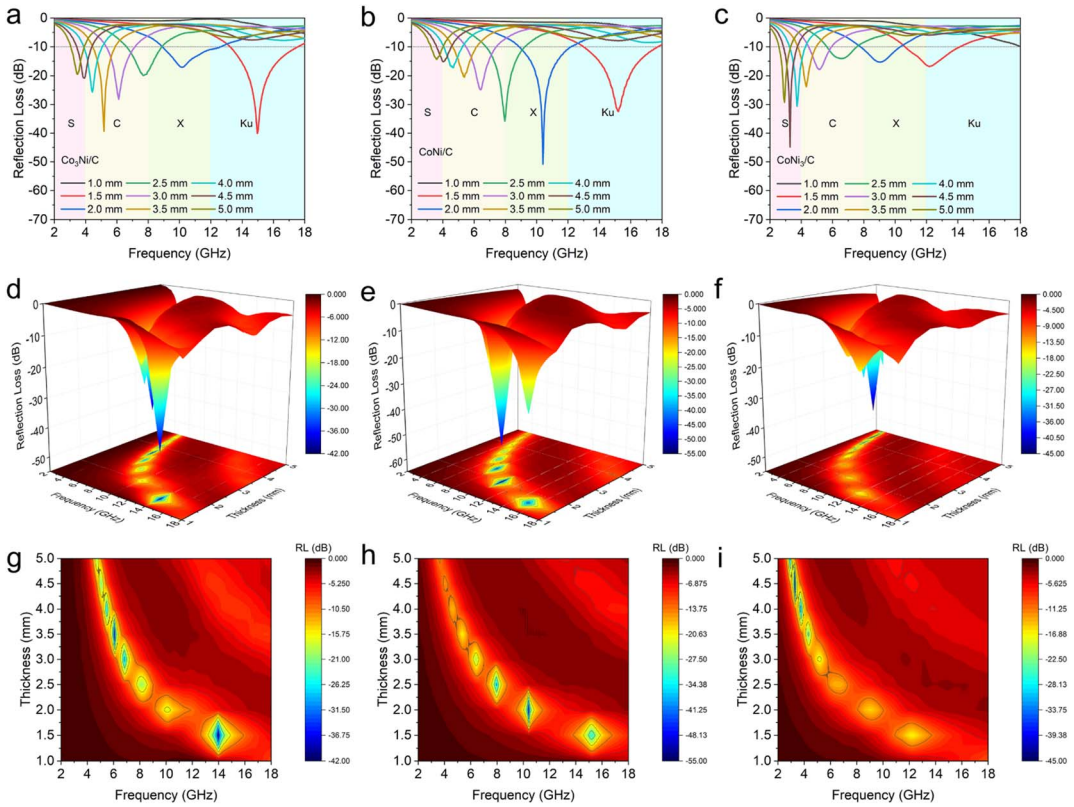

Fig. 5 Calculated RL curves at different thicknesses of (a) Co_3Ni/C, (b) CoNi/C, and (c) $CoNi_3/C$. The corresponding three-dimensional (3D) and contour RL representations of (d and g) Co_3Ni/C, (e and h) CoNi/C, and (f and i) $CoNi_3/C$.

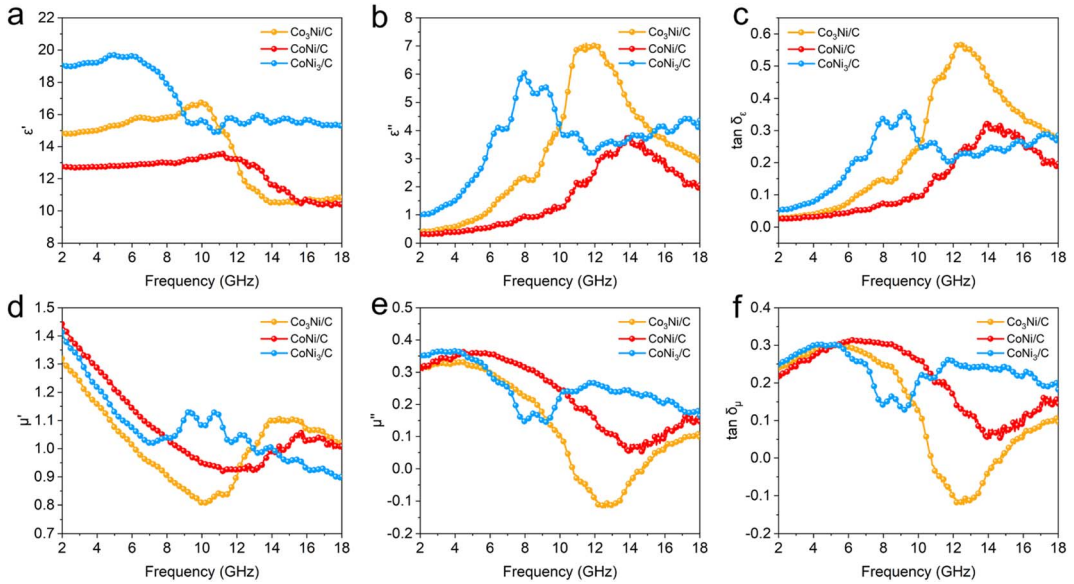

Fig. 6 Electromagnetic parameters of Co_3Ni/C, CoNi/C, and $CoNi_3/C$. (a) The real part (ε') and (b) imaginary part (ε'') of the complex permittivity. (c) Dielectric loss tangents. (d) The real part (μ') and (e) imaginary part (μ'') of the complex permeability. (f) Magnetic loss tangents.

in the low frequency range, implying that magnetic loss plays a predominant role in the lossy mechanism.[28]

Generally, the Debye relaxation theory can be applied to analyze the dielectric polarization relaxation process through the following formula:[40–42]

$$\left(\varepsilon' - \frac{\varepsilon_s + \varepsilon_\infty}{2}\right)^2 + (\varepsilon'')^2 = \left(\frac{\varepsilon_s - \varepsilon_\infty}{2}\right)^2 \quad (3)$$

where ε_s and ε_∞ indicate the static permittivity and the dielectric permittivity at an infinite frequency, respectively. In the ε'–

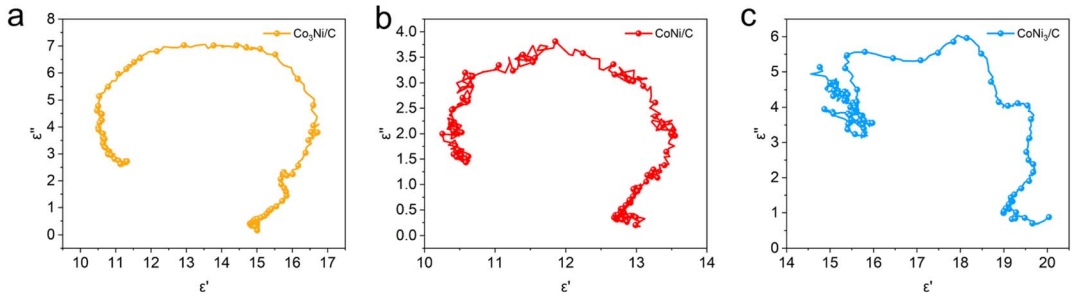

Fig. 7 Cole–Cole semicircles of (a) Co_3Ni/C, (b) CoNi/C, and (c) $CoNi_3/C$.

ε'' plot, the presence of each semicircle, known as the Cole–Cole semicircle, signifies the occurrence of a Debay dipole relaxation process.[40,43] As shown in Fig. 7a–c, Co_3Ni/C, CoNi/C, and $CoNi_3/C$ exhibit multiple Cole–Cole semicircles, indicating the existence of multiple relaxation processes such as interface polarization and dipole polarization.[12,44] Moreover, some irregular Cole–Cole semicircles reflect that there are other mechanisms other than the Debye relaxation theory for the dielectric loss,[45,46] possibly due to heterogeneous interfaces between CoNi alloy and graphite carbon. These interfaces provide abundant phase interface sites, facilitating charge accumulation, dispersion, and repetitious reflection of electromagnetic waves.[9]

4. Conclusions

In summary, we report a facile thermal reduction method to fabricate CoNi bimetallic alloys/carbon composites (Co_3Ni/C, CoNi/C, and $CoNi_3/C$) with irregular rod-like structures. Benefiting from the tunable chemical composition and structure of CoNi-MOFs, the electromagnetic parameters of composites can be effectively controlled by modulating the molar ratio of Co and Ni. In addition, owing to the strong interfacial interaction of CoNi alloy and carbon, the optimized CoNi/C exhibits good impedance matching. As an electromagnetic wave absorber, the CoNi/C with a filler loading of 50 wt% delivers an optimal RL_{min} of −50.80 dB at 10.40 GHz and a maximum EAB of 4.77 GHz at a low thickness of 1.5 mm. Interestingly, the $CoNi_3/C$ also possesses an impressive RL_{min} of −44.84 dB at 3.28 GHz in the S band. The present work provides a feasible method to controllably fabricate MOF-derived MAMs.

Conflicts of interest

There are no conflicts to declare.

Acknowledgements

This work was supported by the Science and Technology Foundation of Lanzhou (2021-1-40), the Central Guidance on Local Science and Technology Development Fund of Gansu Province (23ZYQA314), and the LICP Cooperation Foundation for Young Scholars (HZJJ23-10).

References

1 S. Hou, Y. Wang, F. Gao, H. Yang, F. Jin, L. Ren, Q. Wu, H. Ge and Y. Wang, *Chem. Eng. J.*, 2023, **471**, 144779.
2 C. Wen, X. Li, R. Zhang, C. Xu, W. You, Z. Liu, B. Zhao and R. Che, *ACS Nano*, 2022, **16**, 1150–1159.
3 Y. Li, X. Liu, X. Nie, W. Yang, Y. Wang, R. Yu and J. Shui, *Adv. Funct. Mater.*, 2019, **29**, 1807624.
4 B. Li, Y. Yang, N. Wu, S. Zhao, H. Jin, G. Wang, X. Li, W. Liu, J. Liu and Z. Zeng, *ACS Nano*, 2022, **16**, 19293–19304.
5 M. Cao, X. Wang, W. Cao, X. Fang, B. Wen and J. Yuan, *Small*, 2018, **14**, 1800987.
6 B. Zhao, Y. Li, Q. Zeng, L. Wang, J. Ding, R. Zhang and R. Che, *Small*, 2020, **16**, 2003502.
7 K. Hu, H. Wang, X. Zhang, H. Huang, T. Qiu, Y. Wang, C. Zhang, L. Pan and J. Yang, *Chem. Eng. J.*, 2021, **408**, 127283.
8 K. Cao, X. Yang, R. Zhao and W. Xue, *ACS Appl. Mater. Interfaces*, 2023, **15**, 9685–9696.
9 R. Cheng, Y. Wang, X. Di, Z. Lu, P. Wang, M. Ma and J. Ye, *J. Colloid Interface Sci.*, 2022, **609**, 224–234.
10 N. Wang, Y. Wang, Z. Lu, R. Cheng, L. Yang and Y. Li, *Carbon*, 2023, **202**, 254–264.
11 Y. Liu, Y. Wang, N. Wu, M. Han, W. Liu, J. Liu and Z. Zeng, *Nano-Micro Lett.*, 2023, **15**, 240.
12 Y. Han, J. Yuan, Y. Zhu, Q. Wang, L. Li and M. Cao, *J. Colloid Interface Sci.*, 2022, **609**, 746–754.
13 B. Li, N. Wu, Q. Wu, Y. Yang, F. Pan, W. Liu, J. Liu and Z. Zeng, *Adv. Funct. Mater.*, 2023, **33**, 2307301.
14 T. Zhao, Y. Liu, H. Wan, Z. Li, Y. Wu and H. Yan, *Mater. Chem. Phys.*, 2023, **310**, 128486.
15 Z. Chen, K. Tian, C. Zhang, R. Shu, J. Zhu, Y. Liu, Y. Huang and X. Liu, *J. Colloid Interface Sci.*, 2022, **616**, 823–833.
16 H. Zhang, Y. Zhao, X. Zuo, H. Huang, C. Sun, Z. Fan and L. Pan, *Chem. Eng. J.*, 2023, **467**, 143414.
17 Q. Liu, Q. Cao, H. Bi, C. Liang, K. Yuan, W. She, Y. Yang and R. Che, *Adv. Mater.*, 2016, **28**, 486–490.
18 M. A. Aslam, R. Ahsen, W. Uddin, S. ur Rehman, M. S. Khan, M. Bilal, N. Li and Z. Wang, *Eur. Phys. J. Plus*, 2022, **137**, 480.
19 H. Qiu, X. Zhu, P. Chen, J. Liu and X. Zhu, *Compos. Commun.*, 2020, **20**, 100354.
20 J. Tao, R. Tan, L. Xu, J. Zhou, Z. Yao, Y. Lei, P. Chen, Z. Li and J. Z. Ou, *Small Methods*, 2022, **6**, 2200429.

21 F. Wu, M. Ling, L. Wan, P. Liu, Y. Wang, Q. Zhang and B. Zhang, *Chem. Eng. J.*, 2022, **435**, 134905.
22 Y. Ren, Y. Zhang, Q. Zheng, L. Wang and W. Jiang, *Carbon*, 2023, **206**, 226–236.
23 S. Ren, H. Yu, L. Wang, Z. Huang, T. Lin, Y. Huang, J. Yang, Y. Hong and J. Liu, *Nano-Micro Lett.*, 2022, **14**, 68.
24 X. Zhang, X.-L. Tian, Y. Qin, J. Qiao, F. Pan, N. Wu, C. Wang, S. Zhao, W. Liu, J. Cui, Z. Qian, M. Zhao, J. Liu and Z. Zeng, *ACS Nano*, 2023, **17**, 12510–12518.
25 C. Xu, P. Liu, Z. Wu, H. Zhang, R. Zhang, C. Zhang, L. Wang, L. Wang, B. Yang, Z. Yang, W. You and R. Che, *Adv. Sci.*, 2022, **9**, 2200804.
26 P. Yin, G. Wu, Y. Tang, S. Liu, Y. Zhang, G. Bu, J. Dai, Y. Zhao and Y. Liu, *Chem. Eng. J.*, 2022, **446**, 136975.
27 C. Liu, Z. Zeng, J. Qiao, Q. Wu, W. Liu, F. Gao and J. Liu, *Carbon*, 2023, **213**, 118277.
28 X. Zhang, X. Tian, J. Qiao, X. Fang, K. Liu, C. Liu, J. Lin, L. Li, W. Liu, J. Liu and Z. Zeng, *Small*, 2023, **19**, 2302686.
29 W. Wang, K. Nan, H. Zheng, Q. Li and Y. Wang, *Carbon*, 2023, **210**, 118074.
30 N. He, Z. He, L. Liu, Y. Lu, F. Wang, W. Wu and G. Tong, *Chem. Eng. J.*, 2020, **381**, 122743.
31 Y. Lv, J. Tian, Z. Chen, J. Wang, L.-A. Ma, L. Zhang, S. Chen, Q. Wang and X. Ye, *Chem. Eng. J.*, 2023, **478**, 147413.
32 M. Sun, D. Wang, Z. Xiong, Z. Zhang, L. Qin, C. Chen, F. Wu and P. Liu, *J. Mater. Sci. Technol.*, 2022, **130**, 176–183.
33 L.-L. Liang, Z. Liu, L.-J. Xie, J.-P. Chen, H. Jia, Q.-Q. Kong, G.-H. Sun and C.-M. Chen, *Carbon*, 2021, **171**, 142–153.
34 Z. Su, S. Yi, W. Zhang, L. Tian, Y. Zhang, S. Zhou, B. Niu and D. Long, *Adv. Electron. Mater.*, 2022, **9**, 2201159.
35 W. Ma, R. Yang and T. Wang, *ACS Appl. Nano Mater.*, 2020, **3**, 8319–8327.
36 J. Yang, Z. Liu, H. Zhou, L. Jia, A. Wu and L. Jiang, *ACS Appl. Mater. Interfaces*, 2022, **14**, 12375–12384.
37 X. Meng, L. He, Y. Liu, Y. Yu and W. Yang, *Carbon*, 2022, **194**, 207–219.
38 H. Wang, F. Meng, F. Huang, C. Jing, Y. Li, W. Wei and Z. Zhou, *ACS Appl. Mater. Interfaces*, 2019, **11**, 12142–12153.
39 J. Li, F. Zhang, H. Lu, W. Guo, X. He and Y. Yuan, *Carbon*, 2021, **181**, 358–369.
40 W. Zhang, G. Tan, J. Hu, Q. Wang, W. Yan and Q. Man, *Chem. Eng. J.*, 2023, **478**, 147414.
41 X. Zhang, Y. Zhang, J. He, H. Li, Y. Bai and S. Gao, *Fuel*, 2023, **331**, 125811.
42 X. Wang, P. Ou, Q. Zheng, L. Wang and W. Jiang, *Small*, 2023, 2307473, DOI: **10.1002/smll.202307473**.
43 G. Yu, M. Ye, A. Han, Q. Liu, Y. Su and C. Chen, *J. Alloys Compd.*, 2023, **939**, 168592.
44 X. Wang, J.-C. Shu, X.-M. He, M. Zhang, X.-X. Wang, C. Gao, J. Yuan and M.-S. Cao, *ACS Sustainable Chem. Eng.*, 2018, **6**, 14017–14025.
45 Y. Wang, X. Di, Z. Lu and X. Wu, *J. Colloid Interface Sci.*, 2021, **589**, 462–471.
46 W. Wang, H. Zhang, Y. Zhao, J. Wang, H. Zhao, P. Li, J. Yun, Z. Deng, Z. Zhang, J. Tian, J. Yan, W. Zhao and F. Zhang, *Chem. Eng. J.*, 2021, **426**, 131667.